IEEE Access
Multidisciplinary | Rapid Review | Open Access Journal

SPECIAL SECTION ON SOFT COMPUTING TECHNIQUES FOR IMAGE ANALYSIS IN THE MEDICAL INDUSTRY CURRENT TRENDS, CHALLENGES AND SOLUTIONS

Received December 8, 2017, accepted February 7, 2018, date of publication February 19, 2018, date of current version March 28, 2018.

Digital Object Identifier 10.1109/ACCESS.2018.2807807

Super-Resolved Ultrasound Echo Spectra With Simultaneous Localization Using Parametric Statistical Estimation

KONSTANTINOS DIAMANTIS[1], ARIS DERMITZAKIS[2], JAMES R. HOPGOOD[3], (Member, IEEE), AND VASSILIS SBOROS[1]

[1]Institute of Biological Chemistry, Biophysics and Bioengineering, Heriot-Watt University, Edinburgh EH14 4AS, U.K.
[2]Biomedical Technology Unit, Department of Medical Physics, University of Patras, 26504 Patras, Greece
[3]Institute for Digital Communications, School of Engineering, The University of Edinburgh, Edinburgh EH9 3JL, U.K.

Corresponding author: Vassilis Sboros (v.sboros@hw.ac.uk)

This work was supported by the Science and Technology Facilities Council under Grant STFC-ST/M007804/1.

ABSTRACT Ultrasound contrast imaging (UCI) aims to detect flow changes in the vascular bed that can help differentiate normal from diseased tissues thus providing an early screening tool for diagnosis or treatment monitoring. Ultrasound contrast agents (UCAs), used in UCI, are microbubbles that scatter ultrasound non-linearly. To date the signal processing research has successfully subtracted signals from the linear response of tissue (linear signals), but, in general, has not provided a sensitive detection that is specific to the UCA signal. This paper develops a method for the temporal and spectral estimation of linear and non-linear ultrasound echo signals. This technique is based on non-parametric methods for coarse estimation, followed by a parametric method within a Bayesian framework for estimation refinement. The results show that the pulse location can be estimated to within ± 3 sample points accuracy for signals consisting of ≈ 80 sample points depending on the signal type, while the frequency content can be estimated to within 0.050 MHz deviations for frequencies in the 1 to 4 MHz range. This parametric spectral estimation achieved a 5-fold improvement in the frequency resolution compared with Fourier-based methods, and revealed previously unresolved frequency information that led to over 80% correct signal classification for linear and non-linear echo signals.

INDEX TERMS Bayesian inference, Markov chain Monte Carlo, medical ultrasound, microbubbles, ultrasound contrast imaging.

I. INTRODUCTION

A large number of human diseases are associated with abnormal vascular networks such as cancer, ischaemia, inflammation and also novel therapeutic interventions such as tissue regeneration. The measurement of perfusion and its quantification has been the subject of intensive research across the spectrum of imaging technologies for decades. However, the real time detection and monitoring of perfusion or microvascular flow currently represents a major clinical and research bottleneck and is essential in the understanding, diagnosis, and therapy monitoring of such diseases. Ultrasound contrast imaging (UCI) uses injections of sub-capillary sized microbubbles (MB) stabilized with a biocompatible shell in diameters between $1 - 6\ \mu$m, to ensure image contrast from the vascular bed [1]. Suitably, these MBs remain within the vascular bed and have flow kinetics similar to blood cells. This enables the measurement of vascular and microvascular blood flow using modern ultrasound systems [2], [3]. However, this technology has not achieved quantitative status and, compared to magnetic resonance imaging (MRI) and positron emission tomography (PET), UCI has lower sensitivity and reproducibility and it is highly operator dependent [4]–[7].

Historically, the introduction of MBs to diagnostic ultrasound contrast imaging sparked a debate on their physical behaviour and a number of theoretical models have been proposed [8], [9]. This debate remains open and inconclusive [10]. This is partly due to the high number of parameters that affect the behaviour of MBs and the difficulty in isolating these experimentally. As a result this theoretical debate has not converged into models that can aid the UCI signal processing design. State of the art clinical UCI signal

processing is based on basic amplitude and phase modulation techniques, that successfully suppress linear tissue echo but offer very little in the enhancement or differentiation of non-linear MB signals [11]–[14]. In addition, despite the introduction in the clinic of a few UCI applications (e.g. liver lesion diagnosis), today the MB signal and image processing remain sub-optimal and there are still significant discrepancies between *in-vitro* and *in-vivo* contrast image data that are difficult to interpret [15]. Thus, signal processing tools especially designed for the analysis of echo signals need to be developed. MBs provide ultrasound echoes [13], [14], that can be distinguished from linear scatters such as tissue; statistical properties of these echo returns include total intensity, spectral content, and temporal information. By detecting the presence of UCAs and differentiating them from tissue, the resolution and sensitivity of ultrasound images can be greatly improved to detect vascular activity.

Compared to soft tissue, MBs are more compressible and expandable when insonified with ultrasound. As a result when exposed to ultrasound they oscillate under the varying pressure of the field. This oscillating behaviour results in high scattering strength of the contrast MBs [16]. In the ultrasound literature, soft tissue provides linear scatter, which will be related to the incident field following linear scatter theory. This means that the linear scatter spectra are expected to consist of specific frequency components, with small variations among them. By contrast, MBs usually provide non-linear scatter and they may generate a more variable spectral content including various sub- and ultra-harmonics [17], [18]. Most traditional frequency estimation techniques in ultrasonics are based on the Fourier transform (FT) [19]. The frequency resolution (Δf), i.e. the ability to distinguish two frequency components that are closely-spaced, depends solely on the signal length and the sampling frequency. However, the ultrasound signals are short in duration and the FT results in spectral peaks that are not narrow enough to determine their exact position and number. Moreover, the FT does not localize in time whereas in ultrasonics analysis, the pulse locations and durations are also important.

In previous work [20], [21] a Bayesian spectral analysis technique was introduced providing improved frequency resolution compared to the FT for echo signals from non-linear scatter. Similar results were obtained from a preliminary study on echo signals from linear scatterers [22]. Hence, it is important to investigate whether "hidden" spectral features can be used to identify unclassified scatter received by a transducer. In this study the frequency estimation system is expanded to include temporal information. This was accomplished by incorporating a modified voice activity detection (VAD) technique, mainly used in speech processing [23]–[25]. From the observation of responses from ultrasound scatterers, the pulse location estimation of the echo signals in ultrasound imaging is similar to the signal burst detection in speech detection. However, if the SNR or the amplitudes are low, the performance of the VAD is poor. There is little information in the ultrasonic literature about joint estimation of pulse locations and frequencies system especially for multiple pulse echo signals from MBs [26]. A first study in [27] showed accurate pulse location for MB echo signals on top of the frequency estimation shown in [21] and [22].

The current work builds on the temporal and spectral analysis tools first presented in [21] and [27], by proposing a lower-uncertainty spectral estimator through statistical post-processing of the system's output, and by providing an evaluation of the system performance. The latter was accomplished by testing the system on both synthetic data, and experimentally *in-vitro*, with linear scatterer and non-linear MB ultrasound signals. The findings are discussed with a view to further development of the algorithm as well as to precision improvements in the ultrasound signal characterization.

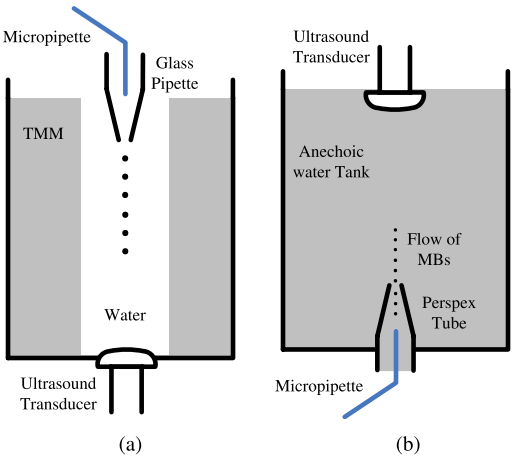

FIGURE 1. Illustration of the experimental setup for echo signal acquisition from (a) SCSs, and (b) MBs.

II. MATERIALS AND METHODS

A. SINGLE ULTRASOUND SCATTER EXPERIMENT

A commercial phased array ultrasound transducer (S3, Philips, Andover, MA, USA) was used to acquire echo signals from solid copper spheres (Goodfellow Cambridge Ltd, Huntingdon, UK) and Definity MBs (Lantheus Inc, MA, USA). The solid copper spheres (SCSs) were used as linear scatterers [11], [28]. All the measurements were carried out using a modified ultrasound scanner (Sonos5500 Philips Medical Systems, Andover, MA, USA). The transmit focus was set to 60 mm depth and the acquisitions were performed between 70 mm and 80 mm depths for both SCSs and MBs, to ensure that the same calibrated settings applied. At this depth range, peak negative pressure of 550 kPa was recorded, ensuring MB survival for more than 50% of the MBs. A 6-cycle sinusoid was used as the excitation pulse with a transmit frequency (f_0) equal to 1.62 MHz. The transducer was not operated at its resonance (around 2.8 MHz), but rather at the low edge of its bandwidth. Data were sampled at 20 MHz and the raw echo signals were stored for further processing. A schematic diagram of the experimental setup, consisting of a water tank and tubing that allowed the flow of SCSs or MBs, is shown in Fig. 1.

In Fig. 1(a), a water tank was used to measure the SCS scatter. This setup was previously used to calibrate the ultrasound receiver at a point in the field in order to provide absolute calibration of microbubble signals [28]. A 4 cm diameter hole at the base of the tank was sealed with a 25 μm thickness Mylar film to provide an acoustic window. The central cylindrical space defined by the circular acoustic window at the base was filled with degassed water. The remainder of the tank was filled with the tissue mimicking material (TMM) [29], in order to minimize multiple reflections. A glass pipette was placed at the top of the tank and its bottom tip with 1 mm internal diameter was held at the center of the tank. Alignment was achieved by aligning a thread inserted through the glass pipette, which was held straight by attaching a lead bead to the bottom. The maximum echo from the thread ensured alignment of the SCS path with the centre of the ultrasound beam. SCSs with a variety of radii, ranging from 29 μm to 58 μm, were dropped individually into the glass pipette, with the help of another micro-pipette, and then into the tank following a path that coincided with the centre of the ultrasound transducer.

The setup for MB echo acquisition (Fig. 1(b)) was similar but with an inverted geometry. The tank was filled with degassed water. A Perspex tube was placed at the center of the bottom of the tank with an 8 mm internal diameter. The tip of a glass micropipette, with approximate diameter 100 μm, was placed at the center of the Perspex tube. The suspension of MBs was diluted enough to ensure the release of single MBs at the tip of the micropipette. The flow in the Perspex tube ensured a MB path at the centre of the ultrasound beam and towards the face of an ultrasound probe, which was placed at the top of the tank.

B. NON-PARAMETRIC TEMPORAL AND SPECTRAL ESTIMATION

Pulse location and spectral estimates using conventional non-parametric estimation (NPE) methods were initially employed to provide the initial conditions for the proposed parametric estimation system. For the pulse localization the Hilbert transform (HT) is commonly used in ultrasound imaging [30] as it enables the extraction of the envelope of the modulated signal [19]. A wavelet denoising (WD) method [31], [32] was also adopted as it presents various advantages compared to traditional filtering approaches in cases of multiple-pulse signals [31], [32]. The combination of the above 2 methods (HTWD) improves the pulse detection accuracy but may fail when there are closely-spaced pulses present in the measured echo signals. The latter was resolved with the addition of a VAD complement [23], [25], and the formation of a joint HTWD-VAD method as presented in [27]. For the spectral estimation, the multi-taper spectrum [33] was chosen to initially analyse the ultrasound signals in the frequency domain [21]. In this technique, several data windows are used on the same data record to obtain a number of modified periodograms, which are averaged to produce a multi-taper spectrum. By reducing the variance, a cleaner spectrum is achieved compared to the Discrete Fourier Transform (DFT).

C. ESTIMATION REFINEMENT

1) PARAMETRIC MODELLING

For the experimentally measured echoes from MBs and SCSs, the number of pulse segments in the signal and the number of frequency components in each pulse segment were all unknown. Based on the excitation pulse used, the multiple pulse-echo signals can be modelled as several segments of sum of sinusoids in noise [34]. It was assumed that there were m pulses in the observed signal with N data points. For each pulse, there are 2 change-points, T_i and T_{i+1}, hence $2m$ change-points in total. A typical MB signal with 9 pulse segments and 2900 points is shown in Fig. 2. The multiple pulses model can be defined as follows:

$$D_0 : x(t) = n(t)$$

$$D_{k_m} : x(t) = \begin{cases} n(t) & \text{if } T_{2i-2} \le t \le T_{2i-1} - 1, \\ x_i(t) + n(t) & \text{if } T_{2i-1} \le t \le T_{2i} - 1, \\ n(t) & \text{if } T_{2m} \le t \le T_{2m+1}, \end{cases}$$

where $i \in (1, m)$, and $x_i(t)$ is given by:

$$x_i(t) = \sum_{j=1}^{k_i} a_{c_{j,k_i}} \cos(\omega_{j,k_i} t) + a_{s_{j,k_i}} \sin(\omega_{j,k_i} t). \tag{1}$$

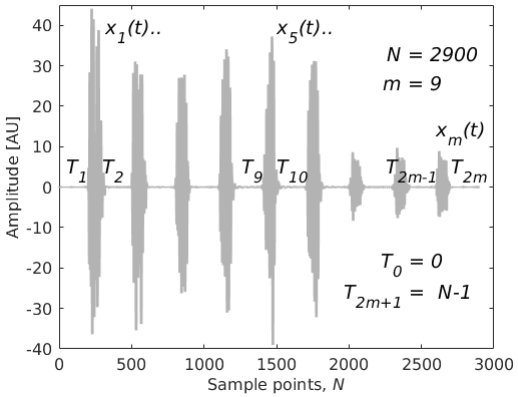

FIGURE 2. Display of an experimental MB raw signal including 9 MB responses in the time domain as recorded after array processing.

Note that the model D_0 corresponds to the lack of any pulses in the observation sequence, and D_{k_m} denotes there are m pulse segments in the signal. The indices $k_1, k_2, \ldots, k_m$ denote the number of super-positioned frequency components in the m pulse segments. In each $i-$th pulse segment, $a_{c_{j,k_i}}$ and $a_{s_{j,k_i}}$ are the cosine and sine amplitudes respectively of the ω_{j,k_i}, that is the $j-$th frequency component of the $i-$th segment with k_i frequency components. Moreover, $n(t)$ is a sequence of a zero mean white Gaussian noise with variance $\sigma^2_{k_i}$. The signal model can be written in vector-matrix form:

$$x = \boldsymbol{G}\left(\boldsymbol{\omega}_{k_m}, \boldsymbol{T}_{2m}\right) \mathbf{a}_{k_m} + \mathbf{n}, \tag{2}$$

where $\mathbf{a}_{k_m} \triangleq [\boldsymbol{a}_{k_1}, \boldsymbol{a}_{k_2}, \ldots, \boldsymbol{a}_{k_m}]^T$, in which $\boldsymbol{a}_{k_i}(i = 1, \ldots, m) \triangleq [(a_{c_{1,k_i}}, a_{s_{1,k_i}}), \ldots, (a_{c_{k_i,k_i}}, a_{s_{k_i,k_i}})]^T$ represents the amplitudes of the frequency components in each pulse segment. $\boldsymbol{G}(\boldsymbol{\omega}_{k_m}, \boldsymbol{T}_{2m})$ is a matrix of non-overlapping elements with a size of $2N \times \sum_{i=1}^{m} k_i$ given by:

$$\mathbf{G} = \begin{bmatrix} 0 & 0 & \cdots & 0 \\ \boldsymbol{G}_1 & 0 & \cdots & 0 \\ 0 & 0 & \cdots & 0 \\ 0 & \boldsymbol{G}_2 & \cdots & 0 \\ 0 & 0 & \cdots & 0 \\ \vdots & \vdots & \ddots & \vdots \\ 0 & 0 & \cdots & 0 \\ 0 & 0 & \cdots & \boldsymbol{G}_m \\ 0 & 0 & \cdots & 0 \end{bmatrix}.$$

The matrix $\boldsymbol{G}$ contains the information about change-points $[T_1, T_2, \ldots, T_{2m}]$, and spectral contents $[\boldsymbol{\omega}_{k_1}, \boldsymbol{\omega}_{k_2}, \ldots, \boldsymbol{\omega}_{k_m}]$ for m different pulse segments. Each component $\boldsymbol{G}_i(i = 1, \ldots, m)$ in the $\boldsymbol{G}$ matrix represents a single pulse where the number of frequency components, the frequency values, their amplitudes, and the noise variance are all unknown parameters. They can all be represented by $\boldsymbol{\theta}_{k_i} \triangleq \left(\boldsymbol{\omega}_{k_i}, \boldsymbol{a}_{k_i}, \sigma_{k_i}^2\right)$. As far as each segment is concerned, the $\boldsymbol{G}_i$ matrix can be defined as:

$$\boldsymbol{G}_i = \begin{bmatrix} E(\omega_{k_1}, T_{2i-1}) & \ldots & E(\omega_{k_i}, T_{2i-1}) \\ E(\omega_{k_1}, T_{2i-1}+1) & \ldots & E(\omega_{k_i}, T_{2i-1}+1) \\ \vdots & \vdots & \vdots \\ E(\omega_{k_1}, T_{2i}-1) & \ldots & E(\omega_{k_i}, T_{2i}-1) \end{bmatrix}$$

where $E(\cdot) \triangleq [\cos(\cdot), \sin(\cdot)]$. Moreover, T_{2i-1} and T_{2i} are the two corresponding change-points for each pulse segment.

2) JOINT POSTERIOR DISTRIBUTION

The Bayesian posterior probability for the frequencies of a signal provides an accurate estimation of frequency peaks [35]. According to Bayesian inference, samples from the posterior distribution can be drawn given the appropriate prior distributions. These priors reflect the degree of belief of the relevant values of the parameters. The joint prior distribution can be considered as the product of the independent parameter priors, displayed in Table 1 for the m segments.

TABLE 1. Prior distributions for independent parameters.

Parameters	Prior Distributions
T_{2m}	Uniform Distribution
k_m	Truncated Poisson Distribution
$\boldsymbol{\omega}_{k_m}$	Uniform Distribution
$\boldsymbol{a}_{k_m}$	Multivariate Normal Distribution
$\sigma^2_{k_m}$	Jeffrey's uninformative prior
δ_m^2	Inverse Gamma Distribution
Λ_m	Gamma Distribution

In Table 1, Λ_m is the hyperparameter of the number of frequency components k_m, and δ_m^2 is the hyperparameter of the amplitudes $\boldsymbol{a}_{k_m}$. The joint prior distribution can be expressed in (3):

$$\begin{aligned} &p(\{k, \boldsymbol{\theta}_k\}_m, \boldsymbol{T}_{2m}) \\ &= p(\{k, \boldsymbol{a}_k, \boldsymbol{\omega}_k\}_m | \sigma_k^2) p(\sigma_k^2) p(\boldsymbol{T}_{2m}) \\ &\propto \Big(\frac{\Lambda_m^{k_m}}{k_m!} \exp(-\Lambda_m) \times \frac{1}{|2\pi\sigma_k^2 \Sigma_{k_m}|^{1/2}} \times \frac{1}{\pi^{k_m}} \\ &\quad \times \exp[-\frac{\boldsymbol{a}_{k_m}^T \Sigma_{k_m}^{-1} \boldsymbol{a}_{k_m}}{2\sigma_k^2}] \Big) \\ &\quad \times \frac{1}{\sigma_k^2} (\frac{1}{N-1} \frac{1}{N-2} \cdots \frac{1}{N-2m}), \end{aligned} \tag{3}$$

where $\boldsymbol{\Sigma}_{k_m}^{-1} = \delta_m^{-2} G^T(\boldsymbol{\omega}_{k_m}, \boldsymbol{T}_{2m}) G(\boldsymbol{\omega}_{k_m}, \boldsymbol{T}_{2m})$.

The posterior distribution is the product of the joint prior distribution and the likelihood function, which based on the signal model is given by:

$$\begin{aligned} p(x \mid \{k, \boldsymbol{\theta}_k\}_m, \boldsymbol{T}_{2m}) = (2\pi\sigma_k^2)^{-N/2} \times \exp\Big\{ -\frac{1}{2\sigma_k^2} \| x \\ - \mathbf{G}(\boldsymbol{\omega}_{k_m}, \boldsymbol{T}_{2m}) \boldsymbol{a}_{k_m} \|^2 \Big\}, \end{aligned} \tag{4}$$

where m in $\{k, \boldsymbol{\theta}_k\}_m$ represents different pulse segments and $\|A\|^2 \triangleq A^T \cdot A$. The posterior distribution in (5) can be obtained after integrating out the nuisance parameters: amplitudes $\boldsymbol{a}_k$ and noise variance σ_k^2 based on Bayes's rule.

$$\begin{aligned} p(\boldsymbol{T}_{2m}, \{k, \boldsymbol{\omega}_k\}_m | x) \propto (\gamma_0 + x^T \mathbf{P}_{k_m} x)^{-(N+\nu_0)/2} \\ \times \frac{(\Lambda_m / [(\delta_m^2 + 1)\pi])^{k_m}}{k_m!} \end{aligned} \tag{5}$$

where $\mathbf{P}_{k_m} = \mathbf{I}_N - \mathbf{G}(\boldsymbol{\omega}_{k_m} \boldsymbol{T}_{2m}) \mathbf{M}_{k_m} \mathbf{G}^T(\boldsymbol{\omega}_{k_m}, \boldsymbol{T}_{2m}), \mathbf{I}_N$ is the identity matrix with N-by-N dimensions, and $\mathbf{M}_{k_m}^{-1} = \mathbf{G}^T(\boldsymbol{\omega}_{k_m}, \boldsymbol{T}_{2m}) \mathbf{G}(\boldsymbol{\omega}_{k_m}, \boldsymbol{T}_{2m}) + \boldsymbol{\Sigma}_{k_m}^{-1}$.

3) REVERSIBLE JUMP MARKOV CHAIN MONTE CARLO ALGORITHM

The refinement of the model parameters, for both pulse locations and frequency components, using a parametric model with numerical Bayesian method, consisted of two steps in each iteration. First, based on the initial guesses given by aforementioned combination algorithm of the VAD and the HTWD for envelope detection, a random walk perturbation was adopted as the proposal distribution for refinement of the pulse location estimates. Specifically, the update of each change-point depended on its previous value and performed a local exploration of the initial guess, which can be described as:

$$T^* | T \sim \mathcal{N}(T, \sigma_T^2). \tag{6}$$

where T and T^* are previous state and new state of the change-point respectively. $\mathcal{N}(\cdot)$ represents the normal distribution with mean T and variance σ_T^2.

Second, for the frequency estimation, a reversible jump Markov chain Monte Carlo (rjMCMC) algorithm was used to explore the regions around dominant peaks from the

multitaper power spectrum initial guess. After the pulse locations were coarsely estimated, frequency estimation was performed for different pulse segments. Although the posterior distribution was simplified, it was still highly non-linear, which means the closed form of $p(\boldsymbol{T}_{2m}, \{k, \boldsymbol{\omega}_k\}_m|x)$ can not be easily obtained. Therefore, the rjMCMC algorithm was introduced to sample from the complicated joint posterior distribution and then to estimate the multiple pulse locations and frequency contents for each pulse segment simultaneously. An ergodic Markov chain whose equilibrium distribution is the specific joint posterior distribution given by (5) was formulated. The simulation was run long enough to reach the stationary distribution. The reversible jump technique (rjMCMC) allowed to jump between subspaces of different model orders. Based on the obtained samples, the Maximum A Posterior (MAP) estimator was adopted to obtain a mode of the estimated posterior distribution $\hat{p}(k_m|x)$ and $\hat{p}(\boldsymbol{\omega}_{k_m}|k_m, x)$. Then, the desired parameters $(k_m, \boldsymbol{\omega}_{k_m})$ were estimated as:

$$\hat{k}_m|x = \arg\max_{k_m} \hat{p}(k_m|x)$$
$$\hat{\boldsymbol{\omega}}_{k_m}|\hat{k}_m, x = \arg\max_{\boldsymbol{\omega}_{k_m}} \hat{p}(\boldsymbol{\omega}_{k_m}|k_m, x) \quad (7)$$

For each of the m segments, there are three candidate moves to be selected. The *birth* and *death* moves introduce dimension changes according to the state of Markov chain, by randomly proposing a new frequency on $(0, \pi)$, or randomly removing an existing one respectively. The *update* move only refines the frequencies within the same dimension. Details of the birth, death and update moves can be found in [21].

D. DATA ANALYSIS

The Bayesian analysis resulted in a highly multi-modal posterior distribution. This made the interpretation of the algorithm's output difficult and several non-sensible parameter estimates were obtained. Imposing limitations such as $k \leq 20$ in [21] is a partial solution to this problem but higher performance could be achieved if further processing is applied to the rjMCMC frequency estimates. Here, this was accomplished by extracting a reasonable summary of the posterior distribution through clustering and outlier rejection.

An initial processing of a number of synthetic signals using the parametric statistical estimation (PSE) system, enabled comparisons with true pulse locations and frequency components that were known, as well as with estimates derived from non-parametric methods. The algorithm was then set to a large number of realizations ($N_{real} = 500$) when applied to real ultrasound signals, to ensure that there were sufficient data for analysis, since many estimates were ignored during a single-case study. A single realization was also set to a high number of iterations ($N_{iter} = 10000$) to ensure that convergence to a specific model order was achieved. The output data from all realizations were considered for the current processing. They were clustered based on the number of detected frequencies (or else model order, k), so that the marginal posterior distributions of parameters of interest can be considered unimodal. Previous allocation of estimated values in histograms, regardless of the model order [21], was no longer adopted. In this work, realizations with the same number of estimated parameters were grouped in terms of model order and the data from the most frequent model order were chosen for further processing. These enabled the calculation of the mean frequency values and the associated standard deviation by applying normal distribution fits to the data from all the realizations of this model order. Frequency estimates referring to the same frequency component (i.e. the first or the last) may contain values that differ greatly from realization to realization. For this reason all values significantly higher than two times the standard deviation were removed.

The pulse location estimation as well as the frequency estimation based on the post-processing described above were followed for an ultrasound transmit pulse, the MB signal of Fig. 2 containing 9 MB pulses, and also 9 SCS individual responses for comparison. The underlying hypothesis here was that super-resolved spectra are possible to extract using this methodology and that real short duration signals provide a reproducible super-resolved spectrum. Ultrasound linear scatter has a well-defined spectrum and was used here to provide this test. The frequency estimates from the transmit pulse were used as a standard of comparison for all the linear and non-linear ultrasound responses. The frequency estimates from all the MB and the SCS responses were then analysed in an attempt to classify any given response into one of the two categories. Specific features in common for most SCS or MB responses revealed initially by the PSE, and subsequently by the use of data-fitting functions were exploited in order to create N_d data points that render the classification possible. A standard k-means algorithm was employed to solve this clustering problem [36]. The number of clusters (N_{cl}) was 2 and therefore two centroids (c) were eventually estimated. Each data point belonging to either a SCS or MB response was associated to the nearest centroid. The S function is a measure of the distance of all data points from their centroids and is given by:

$$S = \sum_{p=1}^{N_{cl}} \sum_{q=1}^{N_d} \| d_q^{(p)} - c_p \|^2, \quad (8)$$

where $\| d_q^{(p)} - c_p \|$ is the Euclidean distance between a data point $d_q^{(p)}$ and the centroid c_p. The algorithm was repeated several times until the centroids no longer change and the squared error function (S) was minimized.

III. RESULTS: ESTIMATION ALGORITHM

A. ESTIMATION OF SYNTHETIC SIGNALS

A synthetic signal was used for an initial performance evaluation of the estimation algorithm. The signal included two pulse segments and consisted of 1500 sample points. As an exemplar, white Gaussian noise with an SNR = 5 dB was also added to the signals. The sampling frequency, f_s, was 20 MHz, and the two pulse segments were synthesized as

a sum of 2 and 3 frequency components, respectively. The two pulses were located between samples (450, 600) and (750, 850) with frequency components (in MHz) at ($0.6\pi = 1.885$, $0.7\pi = 2.199$) and ($0.2\pi = 0.628$, $0.3\pi = 0.943$, $0.32\pi = 1.005$) respectively. The estimation procedure was repeated for 100 times with different noise realizations, amplitudes, and phase components. A paradigm of such a synthetic signal is shown in Fig. 3(a). The 2^{nd} segment was shorter than the first (100 sample points instead of 150). Given the f_s, all Fourier-based methods result in a Δf comparable to 20 MHz/100 = 0.200 MHz [37]. As a consequence, the two larger frequencies separated by 0.062 MHz were regarded as a single frequency by non-parametric analysis (Fig. 3(b)).

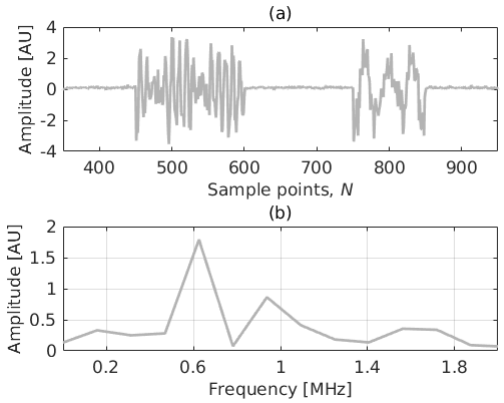

FIGURE 3. (a) Display of a synthetic signal consisting of two pulse segments. (b) Fast Fourier Transform (FFT) of the 2^{nd} segment.

The pulse locations from both NPE and PSE are compared in Table 2. The NPE resulted in less-accurate average estimates for the starting points of both pulses (1^{st} and 3^{rd} change-points), where a 10 point standard deviation (SD) from the true values was measured. By using the parametric method the accuracy of the pulse location estimates improved significantly with standard deviations no higher than 2 sample points, for both pulses, between the different signals. The results confirmed the higher accuracy of the parametric estimation in cases of lower SNRs. Fig. 4 shows the pulse location convergence diagnostics for the 2^{nd} pulse (3^{rd} and 4^{th} change-points) of a single synthetic signal and thus single algorithm realization, as an example. The pulse location estimates were in this case 750 and 849 for the 3^{rd} and 4^{th} change-point, respectively (Fig. 4). The first value (750) was observed with probability of ≈ 0.5, clearly standing out from other estimates (≈ 0.2 at best). The second value (849) was observed with a probability of ≈ 0.42 while the probability of the second most frequent estimate (850) was also relatively high (0.34). Both estimates were within the range described in Table 2. After the first 1000 iterations, all the change-points, related to the start and end points of pulses, reached their stationary distributions.

Each rjMCMC realization detected a specific number of frequencies for each pulse segment as shown in Fig. 5.

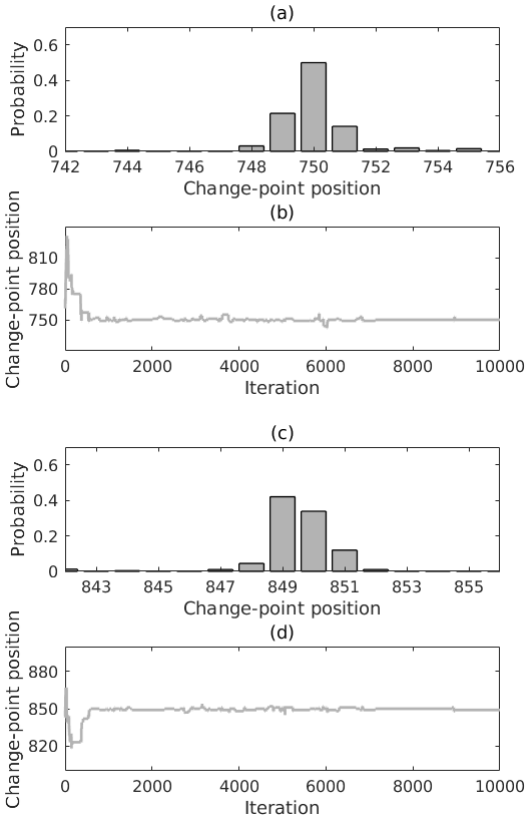

FIGURE 4. Localization of the second pulse segment of a single synthetic signal. Histogram of position and convergence diagnostics are shown in (a) and (b) for the 3^{rd} change-point, and in (c) and (d) for the 4^{th} change-point respectively.

TABLE 2. NPE and PSE (Mean ± SD in sample points) of pulse locations for 100 synthetic signals of varying noise, amplitude and phase. (a) Change-points comparison for the 1^{st} pulse segment. (b) Change-points comparison for the 2^{nd} pulse segment.

Change-point	Ground truth	NPE	PSE
1^{st}	450	460 ± 1	452 ± 2
2^{nd}	600	602 ± 4	600 ± 0

(a)

Change-point	Ground truth	NPE	PSE
3^{rd}	750	760 ± 2	749 ± 1
4^{th}	850	850 ± 1	850 ± 1

(b)

For the 1^{st} segment, the most frequent number of frequencies was 2 and for the 2^{nd} segment, the most common value is 3. The detection of the 3^{rd} component indicates the robustness of the new algorithm. Similar to the pulse locations, the frequency values obtained from 100 realizations using the PSE for the two pulse segments of the synthetic signal were compared to the ground truth, and to the results using NPE (Table 3). Both the non-parametric and the parametric methods provided accurate frequency estimates, for the first pulse segment as shown in Table 3(a). However, the SD values

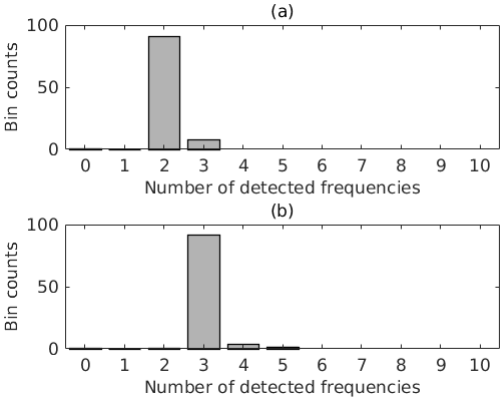

FIGURE 5. Histogram showing the number of detected frequencies using a synthetic signal with 100 randomly selected noise, amplitude, and phase components for (a) the first and (b) the second pulse segment. A single rjMCMC realization was performed on the synthetic signal with a random component set, thus 100 rjMCMC realizations in total.

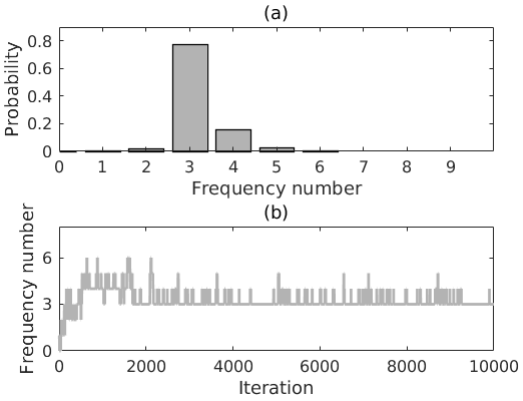

FIGURE 6. (a) Histogram of detected frequencies and (b) convergence diagnostics for the 2^{nd} pulse segment of a single synthetic signal, from a single rjMCMC realization.

TABLE 3. FFT peaks and PSE (Mean ± SD in MHz) for a synthetic signal of 100 randomly selected noise, amplitude and phase components. (a) Frequency estimates comparison for the 1^{st} pulse segment. (b) Frequency estimates comparison for the 2^{nd} pulse segment.

Freqs.	Ground truth	FFT peaks	PSE
1^{st}	2.199	2.200 ± 0.036	$2.199 \pm < 0.001$
2^{nd}	1.885	1.887 ± 0.053	1.885 ± 0.001

(a)

Freqs.	Ground truth	FFT peaks	PSE
1^{st}	0.628	0.620 ± 0.210	$0.629 \pm < 0.001$
2^{nd}	0.943	0.979 ± 0.220	0.939 ± 0.001
3^{rd}	1.005	0.0	1.003 ± 0.001

(b)

were almost two orders of magnitude lower for the parametric method compared to the non-parametric one. In Table 3(b) for the second pulse segment, the NPE can identify two frequency components where the 2^{nd} was estimated between the 2^{nd} and the 3^{rd} true frequency values. On the other hand, not only did the PSE provide estimates closer to the true values, but it was also able to distinguish the two closely-spaced frequencies.

Fig. 6 shows the histogram of detected frequencies and the convergence diagnostics for the 2^{nd} pulse of a single realization, as an example. The most frequent value (3) was observed with probability of 0.78, with significant difference from number 4 which was the second most common estimate with a probability of 0.16. It can be seen that the number of detected frequencies converged to the number 3 after about 2000 iterations. As a result of this convergence, the first 2000 iterations can be considered as the burn-in period.

B. ESTIMATION OF AN ULTRASOUND TRANSMIT PULSE

Fig. 7(a) displays an ultrasound transmit pulse (Tx). The pulse had a duration of ≈ 4 μs which translated to ≈ 80 sample points, given the f_s used here. This resulted in a Δf comparable to 20 MHz/80 $=$ 0.250 MHz when using non-parametric methods for spectral estimation. The proposed estimation system was applied 500 times to the signal. The two change-points, as estimated using the parametric pulse localization system are also shown in Fig. 7(a) together with their standard deviations. The start of the pulse was located at sample point 24 ± 1 (or 1.2 μs) and the end at sample point 96 ± 1 (or 4.9 μs). Importantly a single start and a single end point were found at sample points 30 (or 1.5 μs) and 120 (or 6.1 μs), respectively, using the non-parametric estimation. These were not a good estimate of the pulse edges as displayed in Fig. 7(a). Each of the 500 rjMCMC realizations provided detections of specific number of frequencies for the transmit pulse as shown in Fig. 7(b). The most probable number of frequencies (model order) was $k = 10$, which accounted for 76.4% of the realizations, while the number 11 for 20%. The frequency estimates from the rjMCMC realizations that resulted in $k = 10$ were further processed using histograms. These frequency distribution histograms are displayed in Fig. 7(c), together with their normal distribution fits from where it was possible to calculate mean frequency values and their corresponding standard deviations. The result is shown in Table 4 and also overlaid to the FFT in Fig. 7(d). Given the Δf limitation, the FFT did not result in more than 6 peaks. The transmit pulse broadly looks like a windowed pure sinusoid, and therefore by Fourier analysis side-lobes are expected. Since there is uncertainty in the start and end of the pulse, some of (but not all) the additional frequencies in Fig. 7(c) effectively represent frequencies in these side-lobes, although these components will have small corresponding amplitudes.

Table 4 shows that instead of a single fundamental frequency at 1.62 MHz, which was the f_0 used here, the PSE returned two components around the f_0. A clean single sinusoidal signature was not expected due to the extreme f_0 choice as described in subsection II-A. These two components were $f_1 = 1.562$ (± 0.024) MHz and $f_2 = 1.717$ (± 0.026) MHz and their corresponding harmonics ($h_x \approx 2 \times f_x$, where $x = 1, 2$) were the last two frequencies of the spectrum,

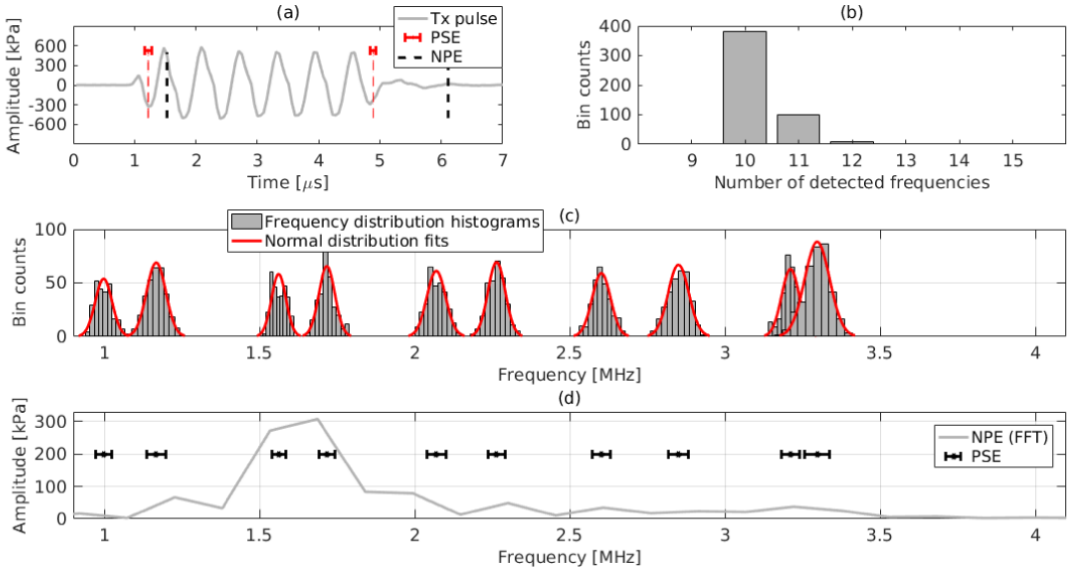

FIGURE 7. (a) Display of a 6-cycle ultrasound transmit pulse in the time domain. The pulse locations found by using the PSE system, as well as by the NPE are also indicated. (b) Histogram showing the number of detected frequencies, and (c) frequency distribution histograms and their normal distribution fits using 500 rjMCMC realizations. (d) FFT of the transmit pulse and mean frequency estimates with their standard deviation obtained by the PSE system.

TABLE 4. PSE for an ultrasound transmit pulse (Mean ± SD in MHz).

Frequencies	Transmit pulse
1^{st}	0.998 ± 0.027
2^{nd}	1.167 ± 0.031
3^{rd}	1.562 ± 0.024
4^{th}	1.717 ± 0.026
5^{th}	2.070 ± 0.030
6^{th}	2.264 ± 0.028
7^{th}	2.602 ± 0.030
8^{th}	2.850 ± 0.033
9^{th}	3.211 ± 0.028
10^{th}	3.297 ± 0.041

$h_1 = 3.211$ (± 0.028) MHz and $h_2 = 3.297$ (± 0.041) MHz, respectively. These two frequency pairs ($f_1 - f_2$, $h_1 - h_2$) and others from the Table 4 (i.e. 5^{th} and 6^{th}) were separated by less than 0.250 MHz, and thus they were not resolved by NPE. By using the rjMCMC algorithm and the processing described in subsection II-D, the Δf was reduced to 0.086 MHz which was the distance between the most closely spaced estimated frequencies (9^{th} and 10^{th}). Further, it is seen from Table 4 that SD values were kept below 0.041 MHz at all cases.

C. ESTIMATION OF SCS RESPONSES

Fig. 8(a) displays an example of a typical SCS response. This entire signal, received by the ultrasound transducer, consisted of $\approx$ 1500 sample points and included a single pulse segment of $\approx$ 80 sample points (or $\approx$ 4 μs duration), similar to the transmit pulse. The two change-points, as estimated using the parametric pulse localization system are also shown in Fig. 8(a), together with their standard deviations. The start of the pulse was located at sample point 580 ± 2 (or 29 μs) and the end at sample point 655 ± 3 (or 32.75 μs). The SD values were slightly increased in the SCS signal (up to 3 sample points) compared to the transmit pulse localization (1 sample point). The equivalent start and end points using the NPE were found at sample points 590 (or 29.5 μs) and 660 (or 33 μs), respectively (Fig. 8(a)). Each of the 500 rjMCMC realizations provided the detections of a specific number of frequencies as shown in Fig. 8(b). The most probable number of frequencies (model order) was $k = 10$, which accounted for 69.2% of the realizations, while the number 11 accounted for 25.2%. All frequency estimates from the rjMCMC realizations that resulted in $k = 10$ are displayed in the histograms of Fig. 8(c), together with their normal distribution fits. Fig. 8(d) displays the resulting mean frequency and standard deviation values alongside the FFT of the SCS response. The latter as in the transmit pulse case, did not reveal more than 6 peaks. The frequency estimates of Fig. 8(d) using the PSE are shown in Table 5 (SCS1), where the equivalent estimates of the other 8 SCS responses can also be found.

Table 5 shows that the PSE resulted in between 9 and 11 frequency components for all SCS responses, which is comparable to the number found in the transmit pulse. These results show that the SCS responses were reproducible and that 9 responses are an adequate sample size to describe their distribution. The fundamental frequency values found were consistently similar to those of the transmit pulse. Specifically, the PSE returned a single frequency component between 1.506 MHz (SCS3) and 1.619 MHz (SCS8), for all SCS responses. The mean and SD values of these

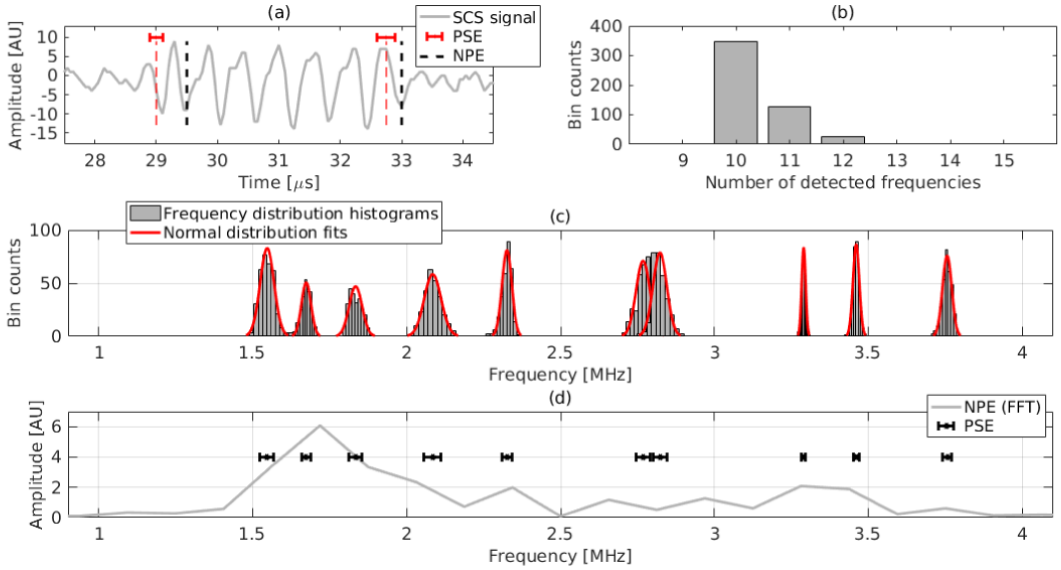

FIGURE 8. (a) Display of an experimental SCS response in the time domain. The pulse locations found by using the PSE system, as well as by the NPE are also indicated. (b) Histogram showing the number of detected frequencies, and (c) frequency distribution histograms and their normal distribution fits using 500 rjMCMC realizations. (d) FFT of the SCS signal and mean frequency estimates with their standard deviation obtained by the PSE system.

TABLE 5. PSE for 9 SCS responses (Mean ± SD in MHz).

Freqs	SCS1	SCS2	SCS3	SCS4	SCS5	SCS6	SCS7	SCS8	SCS9
1^{st}	1.547 ± 0.023	1.253 ± 0.006	1.307 ± 0.043	1.391 ± 0.064	1.379 ± 0.098	1.364 ± 0.106	1.205 ± 0.011	1.619 ± 0.056	1.554 ± 0.147
2^{nd}	1.674 ± 0.015	1.558 ± 0.012	1.506 ± 0.022	1.512 ± 0.038	1.590 ± 0.039	1.602 ± 0.044	1.610 ± 0.007	1.715 ± 0.063	1.694 ± 0.077
3^{rd}	1.834 ± 0.021	1.757 ± 0.015	1.740 ± 0.017	1.751 ± 0.022	1.779 ± 0.029	1.781 ± 0.031	1.817 ± 0.032	1.772 ± 0.090	1.893 ± 0.047
4^{th}	2.085 ± 0.027	2.005 ± 0.029	2.106 ± 0.063	2.148 ± 0.056	2.051 ± 0.072	2.046 ± 0.077	2.011 ± 0.049	1.977 ± 0.147	1.986 ± 0.098
5^{th}	2.326 ± 0.016	2.165 ± 0.055	2.306 ± 0.051	2.273 ± 0.048	2.212 ± 0.083	2.258 ± 0.092	2.423 ± 0.065	2.304 ± 0.155	2.361 ± 0.081
6^{th}	2.768 ± 0.023	2.366 ± 0.023	2.583 ± 0.078	2.658 ± 0.074	2.396 ± 0.076	2.433 ± 0.078	2.588 ± 0.060	2.447 ± 0.111	2.653 ± 0.077
7^{th}	2.823 ± 0.023	2.607 ± 0.051	2.684 ± 0.081	2.919 ± 0.055	2.599 ± 0.096	2.658 ± 0.071	2.921 ± 0.027	2.790 ± 0.094	2.888 ± 0.080
8^{th}	3.290 ± 0.006	2.884 ± 0.047	2.959 ± 0.067	3.227 ± 0.031	2.935 ± 0.074	2.887 ± 0.048	3.261 ± 0.007	2.967 ± 0.120	3.255 ± 0.051
9^{th}	3.460 ± 0.011	3.276 ± 0.021	3.260 ± 0.013	3.415 ± 0.013	3.271 ± 0.025	3.271 ± 0.014	3.423 ± 0.006	3.301 ± 0.039	3.308 ± 0.046
10^{th}	3.756 ± 0.015	3.463 ± 0.022	3.458 ± 0.026		3.447 ± 0.020	3.450 ± 0.014	3.756 ± 0.015	3.470 ± 0.033	3.496 ± 0.035
11^{th}		3.759 ± 0.017	3.683 ± 0.021		3.719 ± 0.016	3.729 ± 0.013		3.754 ± 0.024	3.635 ± 0.074

components were 1.566 ± 0.041 MHz. Thus, 4×SD (i.e. 95% of the distribution) corresponded to 10.6% of the mean value. This result is statistically similar to the f_1 (1.562 MHz) of the transmit pulse (subsection III-B). The frequency component closest to the f_2 of the transmit pulse ranged between 1.674 MHz (SCS1) and 1.817 MHz (SCS7) for all SCS responses. The mean and SD values of these components were 1.752 ± 0.044 MHz, with 4×SD corresponding to 10.2% of the calculated mean value. This result is not significantly different to the f_2 (1.717 MHz) of the transmit pulse (subsection III-B).

High reproducibility was found for the two harmonic frequency components, which were approximately in the $2 \times f_x$ range. First, all SCS responses included strictly one frequency component in the narrow range between 3.227 MHz (SCS4) and 3.301 MHz (SCS8). Their mean and SD values were 3.268 ± 0.021 MHz, with 4×SD corresponding to 2.6% of the calculated mean value. Second, a single frequency component for each SCS response was found in the also narrow range between 3.415 MHz (SCS4) and 3.496 MHz (SCS9). Their mean and SD values were 3.454 ± 0.024 MHz, with 4×SD corresponding to 2.8% of the calculated mean value. The two components in these ranges represented a shift to larger values compared to the harmonics h_1 (3.211 MHz) and h_2 (3.297 MHz) of the transmit pulse. Importantly, Table 5 shows that only two frequency components per SCS response were found in the harmonic frequency range, with the exception of SCS9 that resulted in 3. In addition, the SCS8 response included a second spectral signature in the f_2 range. Frequency pairs corresponding to $f_1 - f_2$ (average difference 0.185 ± 0.039 MHz), and $h_1 - h_2$ (average difference 0.186 ± 0.024 MHz) were separated by less than 0.250 MHz, and were therefore resolved only after using the PSE. The minimum Δf measured was 0.053 MHz that was the distance between the 8^{th} and the 9^{th} frequency estimates of the SCS9 response. Table 5 also shows that several frequencies between 2 MHz and 3 MHz were in common for only a group of $3 - 4$ of the SCS responses, and were not repeated in all of them. Further, it is seen that SD values varied from a few kHz to

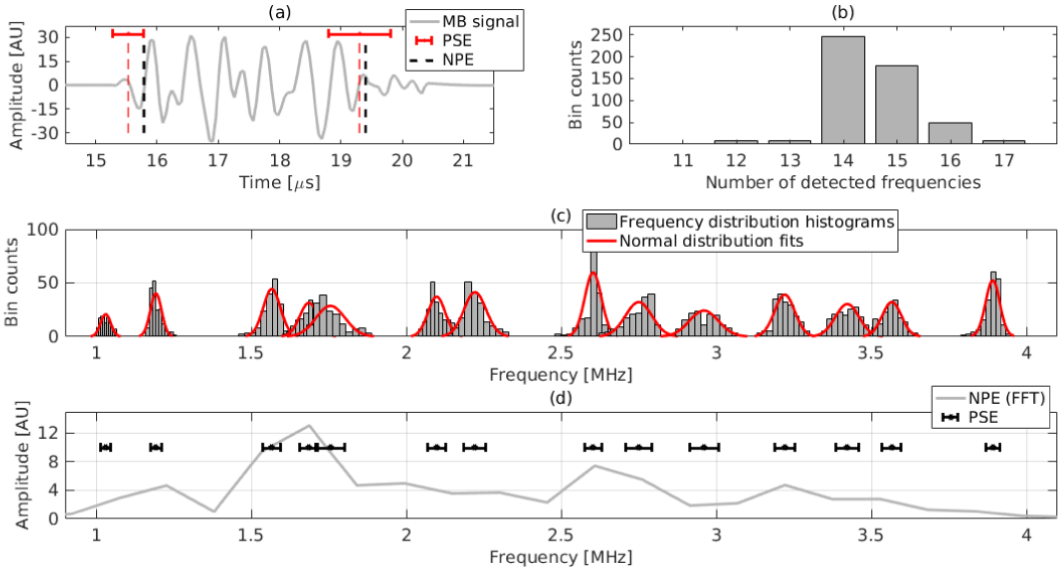

FIGURE 9. (a) Individual display of the second MB response from Fig. 2 in the time domain. The pulse locations found by using the PSE system, as well as by the NPE are also indicated. (b) Histogram showing the number of detected frequencies and (c) frequency distribution histograms and their normal distribution fits using 500 rjMCMC realizations. (d) FFT of the MB response and mean frequency estimates with their standard deviation obtained by the PSE system.

TABLE 6. PSE for 9 MB responses (Mean ± SD in MHz).

Freqs.	MB1	MB2	MB3	MB4	MB5	MB6	MB7	MB8	MB9
1^{st}	0.983 ± 0.021	1.031 ± 0.016	1.127 ± 0.018	1.309 ± 0.048	1.027 ± 0.027	1.266 ± 0.024	1.583 ± 0.020	1.603 ± 0.018	1.562 ± 0.024
2^{nd}	1.147 ± 0.035	1.193 ± 0.018	1.476 ± 0.030	1.425 ± 0.026	1.246 ± 0.035	1.473 ± 0.029	1.704 ± 0.028	1.700 ± 0.029	1.723 ± 0.023
3^{rd}	1.287 ± 0.061	1.567 ± 0.028	1.623 ± 0.027	1.634 ± 0.031	1.453 ± 0.036	1.645 ± 0.037	2.098 ± 0.039	2.193 ± 0.040	2.116 ± 0.035
4^{th}	1.556 ± 0.030	1.686 ± 0.029	1.788 ± 0.045	1.754 ± 0.055	1.654 ± 0.034	1.724 ± 0.068	2.579 ± 0.060	2.262 ± 0.044	2.468 ± 0.040
5^{th}	1.685 ± 0.040	1.756 ± 0.047	2.013 ± 0.043	1.963 ± 0.063	1.783 ± 0.054	1.961 ± 0.057	2.645 ± 0.046	2.364 ± 0.044	2.824 ± 0.089
6^{th}	1.816 ± 0.076	2.098 ± 0.028	2.188 ± 0.046	2.248 ± 0.090	2.010 ± 0.056	2.147 ± 0.110	2.729 ± 0.047	2.853 ± 0.043	2.957 ± 0.092
7^{th}	2.131 ± 0.052	2.222 ± 0.036	2.451 ± 0.080	2.419 ± 0.046	2.192 ± 0.063	2.494 ± 0.097	3.170 ± 0.036	3.164 ± 0.098	3.196 ± 0.051
8^{th}	2.274 ± 0.104	2.603 ± 0.027	2.692 ± 0.035	2.684 ± 0.046	2.437 ± 0.068	2.744 ± 0.094	3.340 ± 0.033	3.239 ± 0.060	3.252 ± 0.025
9^{th}	2.553 ± 0.105	2.750 ± 0.042	2.834 ± 0.044	2.939 ± 0.039	2.626 ± 0.093	3.008 ± 0.042	3.496 ± 0.059	3.361 ± 0.035	3.353 ± 0.034
10^{th}	2.818 ± 0.040	2.960 ± 0.047	3.023 ± 0.037	3.093 ± 0.027	2.964 ± 0.073	3.141 ± 0.031	3.714 ± 0.034	3.476 ± 0.057	
11^{th}	2.934 ± 0.056	3.221 ± 0.032	3.227 ± 0.027	3.208 ± 0.042	3.094 ± 0.042	3.386 ± 0.062			
12^{th}	3.186 ± 0.047	3.422 ± 0.038	3.473 ± 0.017	3.588 ± 0.016	3.265 ± 0.041	3.528 ± 0.034			
13^{th}	3.366 ± 0.035	3.566 ± 0.031		3.863 ± 0.012	3.444 ± 0.066	3.882 ± 0.026			
14^{th}	3.570 ± 0.026	3.891 ± 0.023			3.648 ± 0.050				
15^{th}	3.873 ± 0.022				3.921 ± 0.025				

0.155 MHz. However the larger SD values were associated mainly with the SCS8 response, and the average SD value was 0.049 MHz.

D. ESTIMATION OF MB RESPONSES

The enlarged version for a single pulse segment of Fig. 2, is illustrated in Fig. 9(a) for clarity. This was similar in duration to the transmit pulse or the SCS response shown above ($\approx$ 80 sample points or $\approx$ 4 μs), resulting in the same conventional $\Delta f = 0.250$ MHz. The proposed PSE system was applied 500 times to the MB signal and the results for the segment are shown in Fig. 9. The two change-points, as estimated using the parametric pulse localization system are also shown in Fig. 9(a), together with their standard deviations. The start of the pulse was located at sample point 305 ± 5 (or 15.5 μs) and the end at sample point 379 ± 10 (or 19.3 μs). The SD values were significantly higher (up to 10 sample points) compared to the SCS pulse localization (3 sample points at worst). The equivalent start and end points using the NPE were found at sample points 310 (or 15.8 μs) and 380 (or 19.4 μs), respectively (Fig. 9(a)). Fig. 9(b) displays the number of detected frequencies for the single MB pulse of Fig. 9(a) and for the 500 rjMCMC realizations. The most probable number of frequencies (model order) was $k = 14$, which accounted for 49% of the realizations, while the number 15 accounted for 36%, and the number 16 for 10%. Similar to the previous subsection, all frequency estimates from the rjMCMC realizations for $k = 14$ were further processed. The frequency distribution histograms are displayed in Fig. 9(c), together with their normal distribution fits from where it was possible to calculate mean frequency values and their corresponding standard deviations. Fig. 9(d) displays the resulting mean frequency and standard deviation values alongside the FFT of the MB response. The latter did not reveal more than 7 peaks. The frequency estimates of Fig. 9(d) using the PSE are shown in Table 6 (MB2), where the equivalent estimates of the other 8 MB responses can also be found.

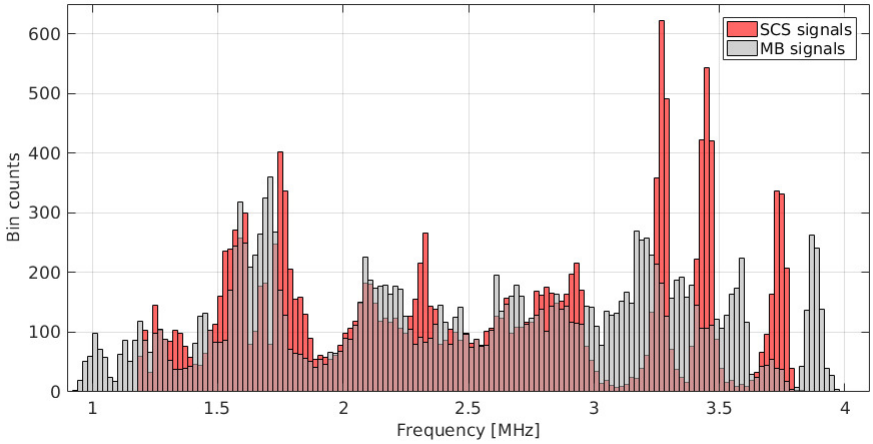

FIGURE 10. Cumulative frequency distribution histograms from 9 MB and 9 SCS responses respectively, using 500 rjMCMC realizations. The bin width was set to 0.020 MHz.

The results from all the different MBs showed that there was reproducibility on these individual frequency signatures but the spread of responses was wider compared to the SCS, and often there was significant overlap between the significant fundamental and harmonic frequencies. Table 6 shows that the PSE resulted in between 8 and 15 frequency components for the 9 MB pulses. This is a much wider range compared to that of the SCS responses. Particularly, the MB responses resulted in a higher number of $>$ 3 MHz frequencies compared to the SCS ones, which made the harmonic frequency definition less straightforward. For the MB2 response, the equivalent to the f_1 frequency was 1.567 ($\pm$0.028) MHz and its harmonic was h_1 = 3.221 ($\pm$0.032) MHz. However, f_2 was not distinct, since the 4^{th} frequency estimate significantly overlapped with the 5^{th} (Fig. 9(c)). Therefore, it was not clear whether f_2 was 1.686 ($\pm$0.029) MHz or 1.756 ($\pm$0.047) MHz. The corresponding harmonic h_2, was also not distinct and both the 12^{th} and the 13^{th} frequencies of the spectrum were candidates. In such cases, the fundamental component (f_x) closest to the transmit one was considered for further analysis. Subsequently, those frequency components closest to 2 times the selected f_x were assumed to be their corresponding harmonics (h_1, h_2). The same processing was followed for all MB responses.

The PSE returned one frequency component between 1.556 MHz (MB1) and 1.654 MHz (MB5), for all MB responses. The mean and SD values values of these components were 1.603$\pm$0.038 MHz. Thus, 4$\times$SD (i.e. 95% of the distribution) corresponded to 9.4% of the mean value. This result is not significantly different to the frequency f_1 (1.562 MHz) of the transmit pulse (subsection III-B). The frequency component closest to the f_2 (1.717 MHz) of the transmit pulse was between 1.685 MHz (MB1) and 1.788 MHz (MB3). The mean and SD values of these components were 1.727$\pm$0.039 MHz, with 4$\times$SD corresponding to 9% of the calculated mean value. The harmonic frequency components that corresponded to $\approx 2 \times f_1$, ranged between 3.141 MHz (MB6) and 3.265 MHz (MB5). Their mean and SD values were 3.206 $\pm$ 0.038 MHz, with 4$\times$SD corresponding to 4.6% of the calculated mean value. This result is not significantly different to the h_1 (3.211 MHz) of the transmit pulse (subsection III-B). Likewise, the harmonic frequency components that corresponded to the $\approx 2 \times f_2$, ranged between 3.366 MHz (MB1) and 3.648 MHz (MB5). Their mean and SD values were 3.468 $\pm$ 0.100 MHz, with 4$\times$SD corresponding to 11.6% of the calculated mean value. This result indicates a shift to larger values compared to the h_2 (3.297 MHz) of the transmit pulse. Note, that in the f_2, h_1, and h_2 ranges there were several MB responses that provided more than one frequency components, thus showing a larger variability compared to the SCS responses. Similar to the SCS spectra, there were several frequencies from the Table 6 separated by less than 0.250 MHz, and were therefore resolved only after using the PSE. The minimum Δf was found to be 0.056 MHz which was the distance between the 7^{th} and the 8^{th} frequency estimates from the results of the MB9 pulse. Importantly Δf was similar to that found in subsection III-C, which demonstrates the consistency of the algorithm. Table 6 also shows that there were a number of frequencies between 2 MHz and 3 MHz, that did not reveal a particular trend between the resulting frequency values of the MB responses. Further, it is seen from Table 6 that all SD values were kept below 0.147 MHz, and the average SD value was 0.045 MHz.

IV. RESULTS: DATA CLASSIFICATION

A. CLASSIFICATION FEATURES

All resulting frequency estimates were put into two separate cumulative histograms one for the SCS and one for the MB responses, with a 0.020 MHz bin width. The two histograms are shown together in Fig. 10. The PSE of the SCS responses showed that most echoes from linear scatterers included specific frequency components, forming relatively

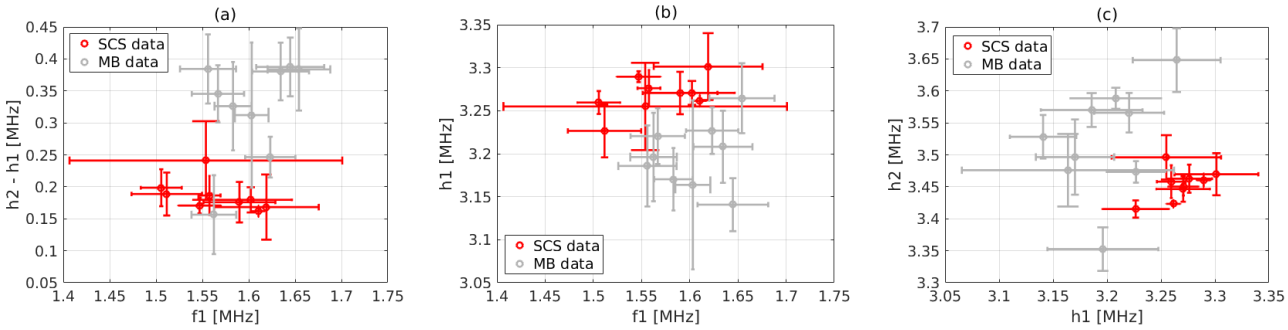

FIGURE 11. Plots for SCS and MB differentiation using various combinations of mean frequency values and their standard deviations obtained by the parametric spectral estimation. (a) The $f1$ is plotted over the $h2 - h1$ difference based on the frequency estimates of the 9 SCS and the 9 MB responses. (b) The $f1$ is plotted over the $h1$ and (c) the $h1$ is plotted over the $h2$.

high and narrow histogram peaks in the frequency ranges primarily between 3 MHz and 3.8 MHz and secondarily between 1.5 MHz and 1.8 MHz. This is related to the fact that in each of the two fundamental and two harmonic signatures there was only one frequency value found, apart from two cases mentioned in subsection III-C. By contrast, the MB frequency values in Fig. 10 were more spread across the bandwidth. There were several less pronounced peaks, that were shorter and broader compared to the SCS population, which reflected the larger variability and overlap in frequency values across the MB responses. These histograms show frequency distribution patterns that may help differentiate the two populations.

TABLE 7. Five highest peaks (Mean ± SD in MHz) from the cumulative frequency distribution histograms including all the rjMCMC realizations for all SCS and MB responses.

Frequencies	SCS	Frequencies	MB
1^{st}	1.573 ± 0.056	1^{st}	1.586 ± 0.037
2^{nd}	1.751 ± 0.029	2^{nd}	1.705 ± 0.044
3^{rd}	3.264 ± 0.021	3^{rd}	3.194 ± 0.092
4^{th}	3.457 ± 0.025	4^{th}	3.585 ± 0.060
5^{th}	3.737 ± 0.027	5^{th}	3.872 ± 0.027

Kernel smoothing functions were employed to fit the data around the 5 most significant spectral peaks of the two histograms [38]. Such functions perform better than normal distribution fits with continuously distributed samples as these shown in Fig. 10. They were used here to confirm the equivalent f_1, f_2, h_1, h_2 frequency components that were obtained from the individual analysis of the SCS and MB responses in subsections III-C and III-D respectively, without taking into account the transmit pulse frequency estimates. This is closer to a real imaging setting, where the knowledge of the transmit pulse is not provided. The mean frequency estimates and their standard deviations derived by the smoothing functions, are shown in Table 7. The first 4 frequency estimates in Table 7 for the SCS responses, compare well to the mean values calculated in subsection III-C, from Table 5. The first 3 frequency estimates in Table 7 for the MB responses, are also not significantly different from the mean values calculated in subsection III-D, from Table 6. Only the 4^{th} frequency estimate (3.585 ± 0.060 MHz) is significantly different from the value calculated in subsection III-D (3.468 ± 0.100 MHz). By visual inspection, the latter value correlates to a lower and wider histogram peak (Fig. 10) between the two peaks which provided the 3^{rd} and 4^{th} mean frequency values in Table 7 for the MB responses. This is an extra indicator of the larger variability across the MB population compared to the SCS one.

B. SCS AND MB DIFFERENTIATION

Mixed plots are shown in Fig. 11 in an attempt to distinguish the MB from the SCS responses and classify any of the 18 given signals as either linear or non-linear scatter. The plots aim to exploit the different frequency values and respective uncertainties found in the SCS and MB populations as described above. In Fig. 11(a) the f_1 frequency was plotted over the $h_2 - h_1$ difference resulting in a concentration of 8 out of 9 SCS data points in a narrow-band area (between 0.15-0.2 MHz) in the centre of the graph. In Fig. 11(b) the f_1 frequency was plotted over the h_1 frequency with the SCS data points concentrated on the centre-top area of the graph. This is a diagonal band for the SCS signals, while the MB population was less clearly defined. However the SCS and MB populations were not fully differentiated, as shown by the errorbar overlap. In Fig. 11(c), the h_1 frequency was plotted over the h_2 frequency resulting in the concentration of most SCS data points in a narrow centre-right region.

Fig. 12 is a similar comparison to that of Fig. 11 including the output from all rjMCMC realizations instead of average values, which enabled classification using a standard k-means clustering method. In Fig. 12(a), the two centroids were calculated to $(1.566, 0.181)$ MHz and $(1.609, 0.374)$ MHz for the SCS and the MB data respectively. The centroids fitted well with the values displayed in Table 7 and resulted in 90.1% correct classification for any given input signal. Similarly, Fig. 12(b) is the equivalent to Fig. 11(b) and includes the signal classification information. The two centroids were calculated to (1.568, 3.268) MHz and (1.604, 3.166) MHz for the SCS and the MB data respectively, and the percentage of correct signal classification is 82.8%. Finally, Fig. 12(c)

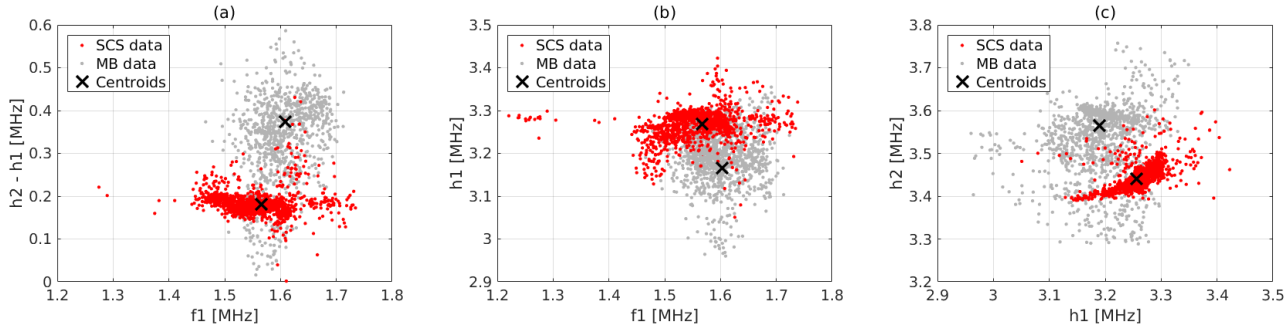

FIGURE 12. Scatter plots and k-means clustering using frequency estimates from all rjMCMC realizations, for the 9 SCS and the 9 MB responses. (a) The $f1$ is plotted over the $h2 - h1$ difference resulting in 90.1% correct signal classification. (b) The $f1$ is plotted over the $h1$ and (c) the $h1$ is plotted over the $h2$ with 82.8% and 88.2% correct signal classification respectively.

corresponded to Fig. 11(c). In this case, the two centroids were calculated to (3.256, 3.441) MHz and (3.189, 3.566) MHz for the SCS and the MB data respectively, and the percentage of correct signal classification was 88.2%.

V. DISCUSSION

The spectral estimation of ultrasound scatter signals can be achieved with high accuracy using parametric methods. Closely spaced frequencies 0.053 MHz apart can be resolved, while the signal duration does not allow less than 0.250 MHz separation for any non-parametric method. These figures are approximately a 5−fold improvement in frequency resolution (Δf). For the example signals examined here, this resulted in double the amount of detected frequencies compared to Fourier Transform based methods. The parametric spectral estimation was particularly efficient in detecting frequencies with low amplitudes in the FFT spectrum, such as all components $>$ 3 MHz in Figs. 7(c), 8(c) and 9(c) (harmonic content). The frequency estimates were also associated with low standard deviations (SD) always below 0.150 MHz and $\approx$ 0.050 MHz on average, for frequency values in the MHz range. These SD values are up to 5 times lower compared to these reported in [21]. The improvement is due to the post-processing which uses a larger number of rjMCMC realizations and separates the frequency estimates based on the model order of each realization (subsection II-D). Such low SD values resulted in revealing: (a) the similarity of the SCS and MB signals with that of the transmit signal in the pair of fundamental frequency components, (b) the fundamental and harmonic components reproducibility across the population of the 9 SCS signals, which also suggests that 9 signals is an adequate sample size for the SCS population in order to characterize its spectral content. These results confirm the linearity of the SCS which had different sizes.

In addition to the automatic spectral estimation, the proposed system allows the simultaneous accurate localization of each pulse. This is expected as it is inherent to the function of the algorithm, i.e. a specific number of frequencies is expected within the bounds of one signal, which helps differentiate with accuracy the time domain of the signal from that of the surrounding noise. This is not the case for non-parametric methods that provide several miscalculations of the signal boundaries, while they are also unable to handle signals including multiple pulses. Therefore, this new method may be part of a robust tool to estimate ultrasound signal information in both time and frequency domains. The linear (SCS) and non-linear (MB) data showed that the super-resolved frequency detection may lead to differentiating their echo signals and classify them into one of the two types successfully even with small sample sizes.

The SCS responses result in a similar number of frequency components (10 ± 1), narrow spectral peaks (Figs. 8(c) and 10) and low standard deviations between the different spectra (Tables 5 and 7) also seen in the transmit pulse (Fig. 7(c)), while in the MB signals the number of frequency components varies and their values tend to overlap (Fig. 9 and Table 6). The increased spread of MB signal response invites further work in this differentiation process. Unlike the SCS, and despite the reproducibility of the specific spectral signature, the MB sample size here is not adequate to characterize its population. Thus, the characterization of a MB population requires a large sample size. However, the comparison and classification using the PSE affords a large number of degrees of freedom such as number of spectral peaks, their values and their estimation uncertainty, and the comparison of all these to the transmit signal. The initial difference in these statistics shown here, was attributed to both the high reproducibility of the SCS responses as well as the variability of the MB responses, and shows promise in the identification of a single signal in the future. The SCS fundamental and harmonic frequency pairs are due to their linear response, fairly similar to those of the transmit pulse. It is not entirely clear why the harmonic location is different to that of the transmit (subsection III-C). Physical processes like non-linear propagation, attenuation and speed of sound variations may play a role and this merits further investigation.

The large variability in the MB responses (Fig. 10) may be attributed to their variable physical behaviour. The varying state of resonance due to the variable MB size distributions in addition to the dispersion of shell mechanical properties (not all MBs of the same size behave the same) [39], may provide

adequate explanation. While the experimental setup is well controlled, in a real ultrasound imaging situation this variability may be further enhanced. First, different locations in the ultrasound beam with different ultrasound field characteristics provide exposure to different field amplitudes and frequencies [40]. Second, the consecutive pulse exposure may result in a varying echo evolution state [12], [13] and third, the different vessel confinements *in-vivo* may also affect the MB response as arteries and veins vary from micrometres to millimetres in diameter [14], [41]. The comparison of the fundamental and harmonic responses from MBs and SCSs (Figs. 11 and 12) is a first step towards utilizing physical understanding in the examination and characterization of their signals, but a much larger sample size is required for broad conclusions. However, the robustness of the methodology suggests that all these results may help elucidate mechanisms that may be possible to quantify using PSE.

Further, the study of single MB acoustics [11], [42] may help develop new UCI signal processing with the aim to enhance the MB response. The detection of MB specific signatures may help in further increasing sensitivity of UCI. This may operate in the context of conventional UCI where large concentrations of microbubbles are injected as a bolus or intravenously, with the aim to provide images of the vascular bed. Specific spectral signatures may be used to further enhance those signals. It is important to note that the theoretical modelling of MB physics behaviour has not been of great assistance to signal processing development. Pulse modulation (amplitude or phase) that is used in current ultrasound contrast modes [17] is more successful in tissue signal cancellation than MB echo enhancement, as its basic aim is set to differentiate linear from non-linear scatter. This is partly due to the inability of the FFT to resolve spectral signature and partly due to the cumulative effect of the above ultrasound propagation factors and MB characteristics that contribute to the echoes within an image pixel, when large MB concentration are utilized. The result should not be significantly different to the cumulative effect presented in Fig. 10, which has provided 90% successful differentiation.

The gains from super-resolved spectral analysis may be more appropriate for single MB processing that is currently the subject of the newly emerging field of super-resolution UCI [43], [44]. The method draws from the localization microscopy and shows potential for an order of magnitude improvement in spatial resolution. It deals with detecting and localizing single MBs, and subsequently tracking them in the vascular bed. Conventional ultrasound transmissions utilize pulses that are short in order to maximize spatial resolution at the expense of frequency resolution. So far these methods are mainly image-based, and may benefit from the technique presented here which has been shown to work well with short duration raw signals. The wide range of MB responses stated above and the ability of the spectral analysis method here to provide high sensitivity information on each individual echo may be beneficial to super-resolution UCI as: (a) the location of the MB pulse can be found accurately and automatically, (b) the MB pulses can be robustly differentiated from linear signals and noise, (c) signal processing may be deployed to adaptively enhance the individual characteristics of each MB and (d) each MB may be recognized thus enabling the identification of the next MB pulse location as a result of consecutive ultrasound exposures, which will improve the identification of their path. In other areas of sensing, it is possible to implement adaptive beamforming methods to create images of improved quality [45]–[47] that will work as an adjunct to the above. This is a developing and exciting area of research for ultrasound imaging.

The current algorithm requires further development in order to provide amplitude, phase and noise estimation. For example, the inclusion of amplitude may remove the ambiguity regarding the definition of fundamental and harmonic frequencies noted here by increasing the degrees of freedom of the comparison and thus resulting in improved signal classification. Further, the capability for pulse localization and separation will be thoroughly characterized and the dependence of the robustness of the technique to the pulse energy, bandwidth and SNR will be understood. The optimization of the algorithm needs to be performed using real diagnostic ultrasound imaging conditions, where the transmit pulse might not available and only the image/signal data can inform this process. Also, conventionally ultrasound transmissions utilize pulses that are as short as possible in order to ensure maximization of spatial resolution. This reduces the available energy and widens the bandwidth in the received signals. Single MB imaging that deploys highly sensitive spectral analysis may afford longer pulse transmission without loss of spatial resolution as localization methods are more dependant on the SNR and less in the pulse duration.

VI. CONCLUSION

This paper presented a novel estimation system for echo signals from linear (solid copper spheres) and non-linear (contrast microbubbles) ultrasound scatter. The parametric model system provided the spectral and temporal parameter estimation simultaneously and automatically within the Bayesian framework. As the posterior density function cannot be solved in a closed form and the dimension of the parameters changes, a reversible jump MCMC algorithm was adopted to give the accurate estimation automatically. To speed up the convergence, a non-parametric coarse estimation for both time and frequency domains was incorporated. The results displayed precise pulse localization compared to that achieved using non-parametric methods that may provide a miscalculation of the change-points of a pulse. In addition, the parametric estimation method provided super-resolved frequency spectra that resulted in increased number of detected frequencies compared to the number of peaks detected by Fourier Transform based methods. Further, the spectra of echo signals from linear and non-linear scatter provided different characteristics, which may be deployed to advance UCI signal processing in the future.

REFERENCES

[1] Q. Wen, S. Wan, Z. Liu, S. Xu, H. Wang, and B. Yang, "Ultrasound contrast agents and ultrasound molecular imaging," *J. Nanosci. Nanotechnol.*, vol. 14, no. 1, pp. 190–209, Jan. 2014.

[2] B. A. Kaufmann, K. Wei, and J. R. Lindner, "Contrast echocardiography," *Current Problems Cardiol.*, vol. 32, no. 2, pp. 51–96, 2007.

[3] E. Quaia, "Microbubble ultrasound contrast agents: An update," *Eur. Radiol.*, vol. 17, no. 8, pp. 1995–2008, 2007.

[4] P. A. Dijkmans *et al.*, "Quantification of myocardial perfusion using intravenous myocardial contrast echocardiography in healthy volunteers: Comparison with positron emission tomography," *J. Amer. Soc. Echocardiogr.*, vol. 19, no. 3, pp. 285–293, 2006.

[5] M.-X. Tang *et al.*, "Quantitative contrast-enhanced ultrasound imaging: A review of sources of variability," *Interface Focus*, vol. 1, no. 4, pp. 520–539, 2011.

[6] C. A. Miller *et al.*, "Voxel-wise quantification of myocardial blood flow with cardiovascular magnetic resonance: Effect of variations in methodology and validation with positron emission tomography," *J. Cardiovascular Mag. Res.*, vol. 16, no. 11, pp. 1–15, Jan. 2014.

[7] F. Pathan and T. H. Marwick, "Myocardial perfusion imaging using contrast echocardiography," *Prog. Cardiovascular Diseases*, vol. 57, no. 6, pp. 632–643, May 2015.

[8] F. Conversano, R. Franchini, A. Lay-Ekuakille, and S. Casciaro, "*In vitro* evaluation and theoretical modeling of the dissolution behavior of a microbubble contrast agent for ultrasound imaging," *IEEE Sensors J.*, vol. 12, no. 3, pp. 496–503, Mar. 2012.

[9] K. Christensen-Jeffries *et al.*, "Microbubble axial localization errors in ultrasound super-resolution imaging," *IEEE Trans. Ultrason., Ferroelect., Freq. Control*, vol. 64, no. 11, pp. 1644–1654, Nov. 2017.

[10] V. Sboros, "A review of single microbubble acoustics," in *Proc. 20th Int. Congr. Acoust. (ICA)*, Aug. 2010, pp. 1–5.

[11] D. H. Thomas *et al.*, "Single microbubble response using pulse sequences: Initial results," *Ultrasound Med. Biol.*, vol. 35, no. 1, pp. 112–119, 2009.

[12] D. H. Thomas *et al.*, "The 'quasi-stable' lipid shelled microbubble in response to consecutive ultrasound pulses," *Appl. Phys. Lett.*, vol. 101, no. 7, p. 071601, 2012.

[13] D. H. Thomas, M. Butler, N. Pelekasis, T. Anderson, E. Stride, and V. Sboros, "The acoustic signature of decaying resonant phospholipid microbubbles," *Phys. Med. Biol.*, vol. 58, no. 3, pp. 589–599, 2013.

[14] D. H. Thomas, V. Sboros, M. Emmer, H. Vos, and N. D. Jong, "Microbubble oscillations in capillary tubes," *IEEE Trans. Ultrason., Ferroelect., Freq. Control*, vol. 60, no. 1, pp. 105–114, Jan. 2013.

[15] A. Needles *et al.*, "Nonlinear contrast imaging with an array-based micro-ultrasound system," *Ultrasound Med. Biol.*, vol. 36, no. 12, pp. 2097–2106, 2010.

[16] S. Hilgenfeldt, D. Lohse, and M. Zomack, "Sound scattering and localized heat deposition of pulse-driven microbubbles," *J. Acoust. Soc. Amer.*, vol. 107, no. 6, pp. 3530–3539, 2000.

[17] E. Stride and N. Saffari, "Microbubble ultrasound contrast agents: A review," *Proc. Inst. Mech. Eng. H, J. Eng. Med.*, vol. 217, no. 6, pp. 429–447, 2003.

[18] A. Greco *et al.*, "Ultrasound biomicroscopy in small animal research: applications in molecular and preclinical imaging," *J. Biomed. Biotechnol.*, vol. 2012, Aug. 2012, Art. no. 519238. [Online]. Available: https://www.ncbi.nlm.nih.gov/pmc/articles/PMC3202139/, doi: 10.1155/2012/519238.

[19] P. Hoskins, K. Martin, and A. Thrush, *Diagnostic Ultrasound: Physics and Equipment*, 2nd ed. Cambridge Univ. Press, 2010.

[20] Y. Yan, J. R. Hopgood, and V. Sboros, "Analysis of echo signal from single ultrasound contrast microbubble using a reversible jump MCMC algorithm," in *Proc. IEEE Eng. Med. Biol. Soc.*, Aug. 2007, pp. 1273–1276.

[21] Y. Yan, J. R. Hopgood, and V. Sboros, "Bayesian spectral estimation applied to echo signals from nonlinear ultrasound scatterers," *EURASIP J. Adv. Sig. Process.*, vol. 2011, p. 146175, Nov. 2010. [Online]. Available: https://doi.org/10.1155/2011/146175

[22] K. Diamantis, M. A. Dhali, G. Gibson, Y. Yan, J. R. Hopgood, and V. Sboros, "Super-resolution spectral analysis for ultrasound scatter characterization," in *Proc. IEEE Int. Conf. Acoust., Speech, Signal Process. (ICASSP)*, Mar. 2016, pp. 903–907.

[23] J.-H. Chang, N. S. Kim, and S. K. Mitra, "Voice activity detection based on multiple statistical models," *IEEE Trans. Signal Process.*, vol. 54, no. 6, pp. 1965–1976, Jun. 2006.

[24] Y. D. Cho, K. Al-Naimi, and A. Kondoz, "Improved voice activity detection based on a smoothed statistical likelihood ratio," in *Proc. IEEE Int. Conf. Acous., Speech, Signal Process. (ICASSP)*, May 2001, pp. 737–740.

[25] J. Sohn, N. S. Kim, and W. Sung, "A statistical model-based voice activity detection," *IEEE Signal Process. Lett.*, vol. 6, no. 1, pp. 1–3, Jan. 1999.

[26] M. Wacker and H. Witte, "Time-frequency techniques in biomedical signal analysis. A tutorial review of similarities and differences," *Methods Inf. Med.*, vol. 52, no. 4, pp. 279–296, May 2013.

[27] Y. Yan, J. R. Hopgood, and V. Sboros, "A novel estimation system for multiple pulse echo signals from ultrasound contrast microbubbles," in *Proc. IEEE Int. Conf. Acous., Speech, Signal Process. (ICASSP)*, Mar. 2008, pp. 601–604.

[28] V. Sboros, S. D. Pye, C. A. MacDonald, J. Gomatam, C. M. Moran, and W. N. McDicken, "Absolute measurement of ultrasonic backscatter from single microbubbles," *Ultrasound Med. Biol.*, vol. 31, no. 8, pp. 1063–1072, 2005.

[29] E. L. Madsen, G. R. Frank, and F. Dong, "Liquid or solid ultrasonically tissue-mimicking materials with very low scatter," *Ultrasound Med. Biol.*, vol. 24, no. 4, pp. 535–542, 1998.

[30] X. A. A. M. Verbeek, L. A. F. Ledoux, P. J. Brands, and A. P. G. Hoeks, "Baseband velocity estimation for second-harmonic signals exploiting the invariance of the Doppler equation," *IEEE Trans. Biomed. Eng.*, vol. 45, no. 10, pp. 1217–1226, Oct. 1998.

[31] X. Lu, R. Liu, J. Liu, and S. Liang, "Removal of noise by wavelet method to generate high quality temporal data of terrestrial MODIS products," *Photogram. Eng. Remote Sens.*, vol. 73, no. 10, pp. 1129–1139, 2007.

[32] G. Soloperto, F. Conversano, A. Greco, E. Casciaro, R. Franchini, and S. Casciaro, "Advanced spectral analyses for real-time automatic echographic tissue-typing of simulated tumor masses at different compression stages," *IEEE Trans. Ultrason., Ferroelect., Freq. Control*, vol. 59, no. 12, pp. 2692–2701, Dec. 2012.

[33] D. G. Manolakis, V. K. Ingle, and S. M. Kogon, *Statistical and Adaptive Signal Processing: Spectral Estimation, Signal Modeling, Adaptive Filtering and Array Processing*. New York, NY, USA: McGraw-Hill, 2000.

[34] P. Stoica and Y. Selen, "Model-order selection: A review of information criterion rules," *IEEE Signal Process. Mag.*, vol. 21, no. 4, pp. 36–47, Jul. 2004.

[35] P. Gregory, *Bayesian Inference and Maximum Entropy Methods in Science and Engineering*. Norwell, MA, USA: Kluwer, 2001.

[36] G. A. F. Seber, *Multivariate Observations*. Hoboken, NJ, USA: Wiley, 1984.

[37] M. S. Lawrence, *Digital Spectral Analysis*. Englewood Cliffs, NJ, USA: Prentice-Hall, 1987.

[38] A. W. Bowman and A. Azzalini, *Applied Smoothing Techniques for Data Analysis*. New York, NY, USA: Oxford Univ. Press, 1997.

[39] D. H. Thomas *et al.*, "Acoustic detection of microbubble resonance," *Appl. Phys. Lett.*, vol. 94, no. 24, p. 243902, Jun. 2009.

[40] V. Sboros, "Response of contrast agents to ultrasound," *Adv. Drug Del. Rev.*, vol. 60, no. 10, pp. 1117–1136, 2008.

[41] M. B. Butler, D. H. Thomas, N. Silva, S. D. Pye, and V. Sboros, "Acoustic detection of microbubble resonance," *Appl. Phys. Lett.*, vol. 99, no. 19, p. 193702, 2011.

[42] D. H. Thomas, M. B. Butler, A. Dermitzakis, T. Anderson, W. N. McDicken, and V. Sboros, "The acoustic scatter from single bisphere microbubbles," *Ultrasound Med. Biol.*, vol. 36, no. 11, pp. 1884–1892, 2010.

[43] M. A. O'Reilly, R. M. Jones, and K. Hynynen, "Three-dimensional transcranial ultrasound imaging of microbubble clouds using a sparse hemispherical array," *IEEE Trans. Biomed. Eng.*, vol. 61, no. 4, pp. 1285–1294, Apr. 2014.

[44] K. Christensen-Jeffries, R. J. Browning, M. X. Tang, C. Dunsby, and R. J. Eckersley, "*In vivo* acoustic super-resolution and super-resolved velocity mapping using microbubbles," *IEEE Trans. Med. Imag.*, vol. 34, no. 2, pp. 433–440, Feb. 2015.

[45] K. Diamantis, I. H. Voxen, A. H. Greenaway, T. Anderson, J. A. Jensen, and V. Sboros, "A comparison between temporal and subband minimum variance adaptive beamforming," *Proc. SPIE Med. Imag. Ultrason. Imag. Tomogr.*, vol. 9040, p. 90400L, Mar. 2014, doi: 10.1117/12.2043602.

[46] K. Diamantis, A. Greenaway, T. Anderson, J. Jensen, P. Dalgarno, and V. Sboros, "Super-resolution axial localization of ultrasound scatter using multi-focal imaging," *IEEE Trans. Biomed. Eng.*, to be published. [Online]. Available: http://ieeexplore.ieee.org/document/8166773/

[47] K. Diamantis, A. Greenaway, T. Anderson, J. A. Jensen, and V. Sboros, "Experimental performance assessment of the sub-band minimum variance beamformer for ultrasound imaging," *Ultrasonics*, vol. 79, pp. 87–95, Aug. 2017.

KONSTANTINOS DIAMANTIS was born in Athens, Greece. He received the Diploma degree in electrical and computer engineering and the M.Sc. degree in biomedical engineering from the University of Patras, Greece, in 2009 and 2011, respectively, and the Ph.D. degree in medical imaging from Heriot-Watt University, Edinburgh, U.K., in 2016. He is currently a Post-Doctoral Research Associate with the Institute of Biological Chemistry, Biophysics and Bioengineering (IB3), Heriot-Watt University. His research interests include array signal processing, adaptive beamforming, statistical signal processing, super-resolution ultrasound imaging, and medical image analysis.

ARIS DERMITZAKIS was born in Athens, Greece. He received the Diploma degree in electrical and computer engineering, the M.Sc. degree in biomedical engineering, and the Ph.D. degree in the field of brain gliomas simulation for use in X-ray imaging techniques from the University of Patras, Greece, in 2007, 2009, and 2014, respectively. He is currently a Post-Doctoral Research Associate with the Biomedical Technology Unit, Department of Medical Physics, University of Patras. His research interests include X-ray imaging simulation, brain modelling and imaging, image processing, ultrasound contrast agents, and ultrasound imaging. He is a member of the Auditing Committee of the Hellenic Society of Biomedical Engineering.

JAMES R. HOPGOOD (M'02) received the M.A. (Hons) and M.Eng. degrees in electrical and information sciences and the Ph.D. degree in statistical signal processing from the University of Cambridge in 1997 and 2001, respectively. He was a Research Fellow with Queens' College Cambridge and the Signal Processing Laboratory, Cambridge University Engineering Department for three years. He joined The University of Edinburgh, Edinburgh, U.K., as a Lecturer in 2004, and then a Senior Lecturer in 2012. He is currently a Senior Lecturer with the School of Engineering, Institute for Digital Communications, The University of Edinburgh. His research expertise include model-based Bayesian inference, speech and audio signal processing in adverse acoustic environments, including blind dereverberation and multi-target acoustic source localization and tracking, single channel signal separation, audio-visual fusion, medical imaging, and blind image deconvolution. Since 2011, he has been an Editor-in-Chief for the *IET Journal of Signal Processing*.

VASSILIS SBOROS was born in Volos, Greece, in 1968. He received the Degree in physics from the University of Athens in 1993 and the M.Sc. degree in medical physics from the University of Aberdeen in 1994, and the Ph.D. degree in ultrasound contrast imaging from The University of Edinburgh in 1999. The jobs that followed investigated the physics of microbubbles and the engineering of imaging them. He has published over 50 peer-reviewed papers. His current research interests include clinical and preclinical ultrasound imaging.